




Broadband THz wave generation in organic benzothiazolium crystals at MHz repetition rates [Invited]

UROS PUC,^{1,3} JEONG-A YANG,^{2,3} DEOKJOONG KIM,² O-PIL KWON,^{2,4,5} AND MOJCA JAZBINSEK^{2,4,*} 

¹*Institute of Computational Physics, Zurich University of Applied Sciences (ZHAW), 8401 Winterthur, Switzerland*

²*Department of Molecular Science and Technology, Ajou University, Suwon 443-749, Republic of Korea*

³*Contributed equally*

⁴*Contributed equally*

⁵*opilkwon@ajou.ac.kr*

**mojca.jazbinsek@zhaw.ch*

Abstract: We present broadband terahertz wave generation based on benzothiazolium crystals at a 100 MHz repetition rate. Among various benzothiazolium crystals, we chose PMB-4TFS (2-(4-(4-(hydroxymethyl)piperidin-1-yl)styryl)-3-methylbenzothiazol-3-ium 4-(trifluoromethyl)benzenesulfonate) due to its large macroscopic optical nonlinearity, good crystal characteristics, and suppressed molecular phonon vibrations. When pumped at the telecommunication wavelength of 1560 nm, the generated THz spectrum covers up to ~15 THz and the corresponding THz amplitude for a 0.29 mm thick crystal at normal incidence is by more than one order of magnitude higher compared to the inorganic standard, 1.0 mm thick ZnTe generator crystal.

© 2022 Optica Publishing Group under the terms of the [Optica Open Access Publishing Agreement](#)

1. Introduction

Terahertz (THz) wave generators are essential device components needed for various THz photonic applications such as linear and nonlinear THz spectroscopy [1,2]. A high THz wave generation efficiency and a broad THz bandwidth are required for a THz wave generator material. Relying on difference frequency generation or optical rectification processes, organic second-order nonlinear optical (NLO) crystals can readily generate broadband THz waves with high amplitude. Compared to inorganic THz crystals such as inorganic NLO crystals, semiconducting and photoconductive crystals (e.g., ZnTe, GaP, and LiNbO₃), benchmark organic NLO crystals exhibit either i) superior macroscopic NLO coefficient, ii) better phase matching between the generated THz wave and the optical pump wave at infrared wavelengths above 1100 nm, or/and iii) lower absorption in the overall 0.1–20 THz frequency range [3]. For instance, in a simple collinear optical rectification geometry at a pump wavelength in the 1300–1500 nm range and a relatively long pulse duration of about 150 fs at kHz-repetition rate, organic styryl-based salt crystals achieve broadband THz wave generation covering over 8 THz and large optical-to-THz conversion efficiency (more than one order of magnitude higher THz amplitude compared to ZnTe) [3,4]. Compared to gas-plasma [5] and metal-spintronic [6,7] THz generators, organic crystalline THz generators can operate in a low-power optical pump regime (in addition to high-power) and/or superior optical-to-THz conversion efficiency. Compared to poled polymer NLO materials [8], organic NLO crystals possess much superior long-term thermal and photochemical stability for high-pulse-energy optical pump beams, as well as much larger interaction lengths necessary for high optical-to-THz conversion efficiency. Therefore, there is a growing interest in organic NLO crystals for efficient, intense, and/or ultra-broadband THz wave generation.

Among various types of organic NLO crystals, molecular salt-type crystals based on highly nonlinear optical styryl-based cationic chromophores have shown many advantages for THz wave generation; large macroscopic second-order optical nonlinearity (e.g., effective first hyperpolarizability [3] in crystals from about 100 to 300×10^{-30} esu), good bulk-crystal growing ability with an area of few square millimeters, optically suitable plate-like morphology with thickness in the ~ 0.1 – 0.5 mm range, and high thermal phase stability [3,9–11]. The thermal phase stability of organic NLO crystals is important for practical THz applications because it determines possible upper and lower operating temperatures and the long-term temporal stability of organic THz generators. For many organic non-ionic NLO crystals, the melting temperature T_m is below 120 °C [12]. Note that the thermal phase stability is limited by phase transition temperatures (e.g., melting temperature T_m or solid-to-solid phase transition temperatures) and by intrinsic thermochemical stability due to the thermal bond-breaking of constituents in crystals.

Recently, new types of organic NLO crystals based on highly efficient styryl-based benzothiazolium cationic chromophores were developed (Fig. 1(a)) [13–17]. A strong electron acceptor, *N*-methyl benzothiazolium was introduced into newly designed cationic chromophores; PMB (2-(4-(4-(hydroxymethyl)piperidin-1-yl)styryl)-3-methylbenzothiazol-3-ium), PFB (5-fluoro-2-(4-(4-(hydroxymethyl)piperidin-1-yl)styryl)-3-methylbenzothiazol-3-ium), and HMB (2-(4-hydroxy-3-methoxystyryl)-3-methylbenzothiazol-3-ium). The corresponding benzothiazolium crystals exhibited either very large diagonal or off-diagonal components of the macroscopic second-order optical nonlinearity and showed excellent performance in first THz wave generation experiments [13–17]. When pumped at infrared wavelengths with a repetition rate of 1 kHz, PMB-based crystals exhibited THz bandwidth up to ~ 8 THz and THz electric field up to 36 times higher than inorganic standard ZnTe crystal with a thickness of 1.0 mm [13]. For benzothiazolium crystals, THz generation and absorption characteristics, and thermochemical stability have not been fully addressed yet.

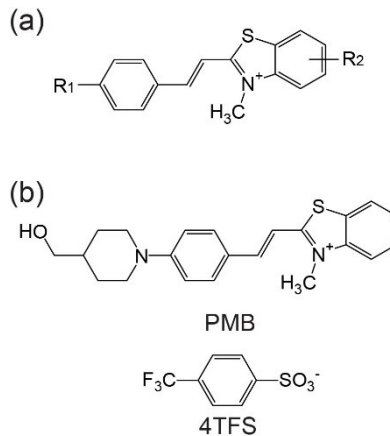


Fig. 1. Chemical structure of (a) benzothiazolium cationic chromophores and (b) PMB cation and 4TFS anion.

In this work, we report broadband THz wave generation based on PMB-based benzothiazolium single crystals at MHz repetition rates. Compared to the previous work at kHz repetition rates [13], we used a compact fiber femtosecond laser source with a relatively very low pump pulse energy of 1.4 nJ. We could achieve a broad THz bandwidth at a comparable signal-to-noise ratio (SNR), important for linear THz time-domain spectroscopy (THz-TDS). A 0.29 mm thick PMB-based crystal broadband THz wave generation covered up to ~ 15 THz when pumped at 1560 nm at a 100 MHz repetition rate. The generated THz electric field was ~ 26 times higher than in the inorganic standard, 1.0 mm thick ZnTe crystal at identical experimental conditions. In addition,

combining thermal analysis with mass spectroscopy, we investigated the thermochemical stability of PMB-based single crystals, as a model example of widely used styryl-based ionic crystals, which is important for designing highly-stable cationic chromophores for highly-efficient organic NLO crystals.

2. Crystal characteristics of PMB-4TFS single crystals

Among various benzothiazolium crystals [13–17], we choose here PMB-4TFS (2-(4-(4-(hydroxymethyl)piperidin-1-yl)styryl)-3-methylbenzothiazol-3-ium 4-(trifluoromethyl) benzenesulfonate) crystals. It is because PMB-4TFS crystals exhibit the largest macroscopic second-order optical nonlinearity with a diagonal component of the effective first hyperpolarizability tensor of about 274×10^{-30} esu, good crystal growing ability with an area of over a few square millimeters and a plate-like morphology, and strong interionic interactions by bis(head-to-tail) complementary assembly for strongly suppressing molecular phonon modes in the THz frequency range. In addition, PMB-4TFS crystals showed excellent THz generation performance at a 1 kHz repetition rate of the optical pump [13].

Under different crystal growth conditions, as-grown PMB-4TFS single crystals show a similar crystal morphology with a plate-like shape. Figure 2 shows photographs of PMB-4TFS single crystals grown by either slow-evaporation or slow-cooling methods in pure and mixed solvent systems. Figure 2(a) shows an example of PMB-4TFS single crystals grown by the slow evaporation method at an evaporation temperature of 30 °C in the methanol and acetonitrile mixture solution (1:1 mol/mol), for which the solution was saturated at 30 °C. Note that the PMB-4TFS single crystal shown in Fig. 2(a) was obtained from the same batch in the growth experiment of PMB-4TFS single crystals used in THz wave generation experiments at a 1 kHz repetition rate in Ref. [13]. Figure 2(b) and 2(c) show a photograph of PMB-4TFS single crystals grown by the slow cooling method in the mixed solvent and pure solvent systems, respectively. The saturation temperature was 41 and 39 °C, respectively. In both solvent systems, the slow-cooling method results in crystal morphology similar to that of the slow-evaporation method. All as-grown crystals exhibit a plate-like shape with the main facet corresponding to the (100) crystallographic plane, which was determined by using reflection X-ray diffraction and considering the single crystal structure from Ref. [13]. In methanol solution, the width of as-grown PMB-4TFS crystals along the crystallographic *b* axis (see also Fig. 3) was narrower than in mixture solution, but the main growth direction was along the *c* axis in all growth experiments in this work.

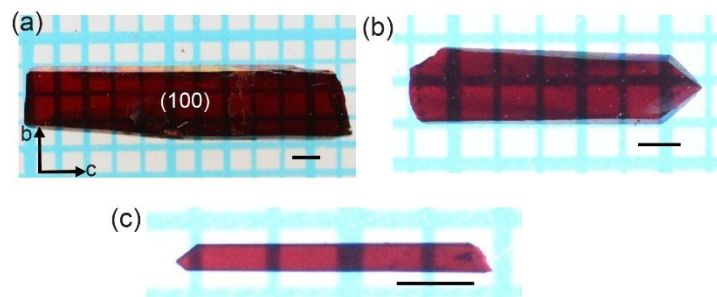


Fig. 2. Photographs of PMB-4TFS single crystals grown by (a) slow evaporation method, (b) slow cooling method in methanol and acetonitrile mixture solution (1:1 mol/mol), and (c) slow cooling method in methanol (scale bar: 1 mm).

Figure 3 shows the molecular ordering of PMB cations and 4TFS (4-(trifluoromethyl) benzenesulfonate) anions in PMB-4TFS crystals exhibiting acentric monoclinic *Cc* space group

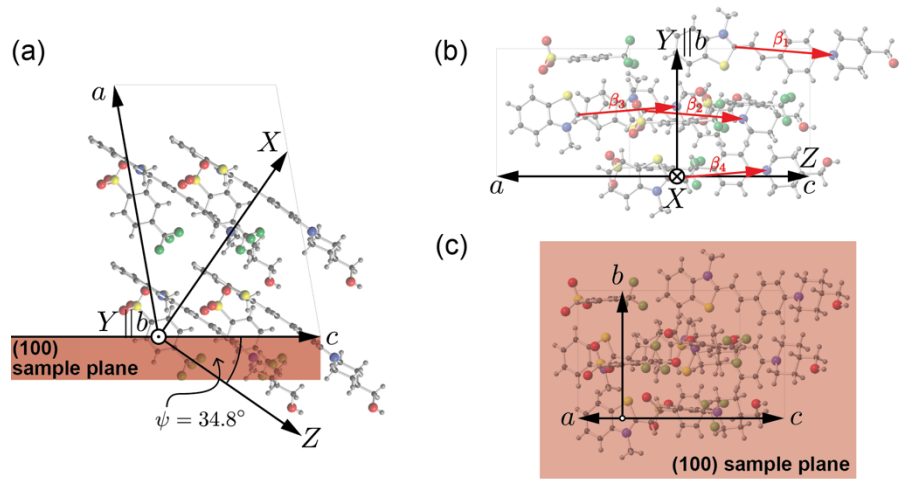


Fig. 3. Molecular packing of one unit cell in PMB-4TFS single crystals with the point group symmetry m and the definition of the dielectric XYZ system in this work: (a) The mirror symmetry ac plane and the orientation of the dielectric X and Z axes in this plane. (b) View along the dielectric X axis normal to the main direction of the first hyperpolarizability β of the chromophores. (c) View normal to the (100) plane (the crystallographic bc plane), which defines the plane of the largest parallel faces of as-grown PMB-4TFS crystals.

symmetry, as measured in Ref. [13] by single crystal X-ray diffraction analysis, and the direction of the dielectric XYZ system with respect to the crystallographic abc system, as used in the present work. The dielectric Y axis is chosen parallel to the crystallographic b axis normal to the mirror symmetry plane according to the usual convention for the crystallographic systems with the point group symmetry m . The cationic chromophores PMB exhibit a very high first hyperpolarizability $\beta = 274 \times 10^{-30}$ esu [13] and the four chromophores in the unit cell are aligned practically parallel with a very small angle of $\theta_p = 4.8^\circ$ to the polar axis Z , which is rotated by about $\psi = 34.8^\circ$ from the crystallographic c axis (Fig. 3(a)). Figure 3(b) shows the view along the dielectric X axis normal to the polar axis Z to show the small angle (4.8°) of the main direction of the first hyperpolarizability β of the four chromophores in the unit cell to the polar axis Z . Note that the main direction of the first hyperpolarizability is here approximated by the direction between the C atom ($N=C-S$) on the electron-acceptor group and the N atom on the electron-donor group of the PMB chromophore. Figure 3(c) shows the view normal to the (100) plane of the as-grown crystals as shown in Fig. 2, which shows a strong alignment anisotropy in this plane with the long molecular axes of both cations and anions along the crystallographic c axis and the short molecular axes along the crystallographic b axis. Due to the highly aligned ordering of the cationic chromophores, the macroscopic second-order susceptibility tensor, according to the oriented-gas model [18] will only have one dominant component $\chi_{ZZZ}^{(2)}$, proportional to the effective first hyperpolarizability of the unit cell $\beta_{ZZZ}^{\text{eff}} = \beta \cos^3 \theta_p = 272 \times 10^{-30}$ esu, while all the other tensor components can be neglected (the maximal off-diagonal component being $\beta_{ZYY}^{\text{eff}} = \beta \sin^2 \theta_p \cos \theta_p \approx 2 \times 10^{-30}$ esu $\ll \beta_{ZZZ}^{\text{eff}}$).

3. THz wave generation

We examined the THz generation characteristics of PMB-4TFS crystals at a 100 MHz repetition rate. The wavelength of the optical pump laser employed was 1560 nm at 38 fs pulse duration and maximum pulse energy of 1.9 nJ. We employed an existing THz-TDS system as described in our previous work [19]. The organic crystal for THz wave generation in the mentioned THz-TDS

system was exchanged with the PMB-4TFS generator crystal with a thickness of 0.29 mm. The pump pulses were incident normal to the as-grown PMB-4TFS crystal surface and polarized along the crystallographic c axis, i.e., along the projection of the polar axis Z to the crystal plane, (100) plane (Fig. 3). The THz detection crystal, 0.76 mm thick DSTMS (4-(4-(dimethylamino)styryl)-1-methylpyridinium 2,4,6-trimethylbenzenesulfonate, from Rainbow Photonics AG) [20] and all other functional aspects of the THz-TDS system were not changed: the polar axis of the THz detection crystal and the polarization of the probe beam were oriented parallel to the polarization of the pump beam; i.e., the THz field generated along the crystal c axis was detected. To reduce the strength of water-vapor absorption lines in the THz spectrum, the time-domain signals were acquired at room temperature in a dry air environment with a relative humidity of about 2%. The acquisition period was 13.3 ps with a temporal resolution of 2 fs (300 nm trigger steps) corresponding to the band limit (Nyquist frequency) of 250 THz. The signals shown in Fig. 4(a) were averaged 200 times and recorded by moving the opto-mechanical delay line at the speed of 300 $\mu\text{m/s}$. In addition, we applied a low-pass FFT filter with a cut-off frequency of 25 THz to the averaged time-domain signal, which removes small high-frequency (~ 190 THz) oscillations in the signal due to the interference of the probe pulses with residual pump optical pulses through the employed filters (0.5 mm thick Ge-wafer and a 20 THz low-pass filter from QMC Instrument Ltd.).

In this configuration, PMB-4TFS crystals generated broadband THz waves with a high THz amplitude. Both time-domain signals in Fig. 4(a) were recorded in the same THz-TDS system where only the generator crystals (PMB-4TFS and ZnTe) were exchanged. The pump pulse energy and the pump fluence at the position of the crystal were 1.4 nJ and 2.3 $\mu\text{J}/\text{cm}^2$, respectively. The 0.29-mm-thick PMB-4TFS crystal generated a peak-to-peak THz amplitude by a factor of ~ 26 times higher compared to the 1.0-mm-thick ZnTe standard benchmark crystal. Note that the amplitude of the ZnTe signal in Fig. 4(a) was multiplied by a factor of 5 for clarity. The generated THz spectrum of PMB-4TFS crystal is in addition very broad, covering up to about 15 THz (Fig. 4(b)) with a peak amplitude of more than one order of magnitude higher than in ZnTe. The dimples of the generated spectra of the PMB-4TFS crystal in Fig. 4(b) originate from the detection limits due to the specific absorption features of the detection crystal and the self-absorption of the generation crystal, as discussed in Section 4.

While most ultra-broadband THz research systems are currently based on bulky and expensive Ti:sapphire femtosecond lasers working at the kHz repetition rate, we use here a compact, ultra-stable pulsed Erbium fiber laser from MenloSystems GmbH operating at the telecommunication wavelength of 1560 nm and five orders of magnitude higher repetition rate of 100 MHz. A high repetition rate along with high stability allows for high signal-to-noise ratios for ultrafast THz spectroscopy applications [21,22], even by using five orders of magnitude lower pump pulse optical energy compared to typical Ti:sapphire kHz systems. Therefore, PMB-4TFS crystals are highly interesting materials for THz wave generation at both MHz- and kHz-repetition rate regimes.

To prove the above-mentioned benefits, we measured the peak-to-peak amplitude as a function of the pump fluence (Fig. 4(c)), showing that both generator crystals employed in this work are used below the saturation point as they respond perfectly linearly. Moreover, the SNR of the acquired signal and consequently the final spectrum is still growing by averaging more signal traces as shown in Fig. 4(d), showing a high stability of the compact THz system.

While we achieve a very high optical-to-THz conversion efficiency compared to ZnTe, there is still potential for further improvement with PMB-4TFS crystals. Since the as-grown crystal morphology is a plate-like with (100) main faces, at normal incidence of the pump beam we only exploit an effective second-order nonlinearity. The optimal crystal cut is expected to be along the YZ dielectric plane, which would exploit the full $\chi_{ZZZ}^{(2)}$ susceptibility tensor element (or the dominant diagonal component of the effective first hyperpolarizability tensor β_{ZZZ}^{eff}). Considering

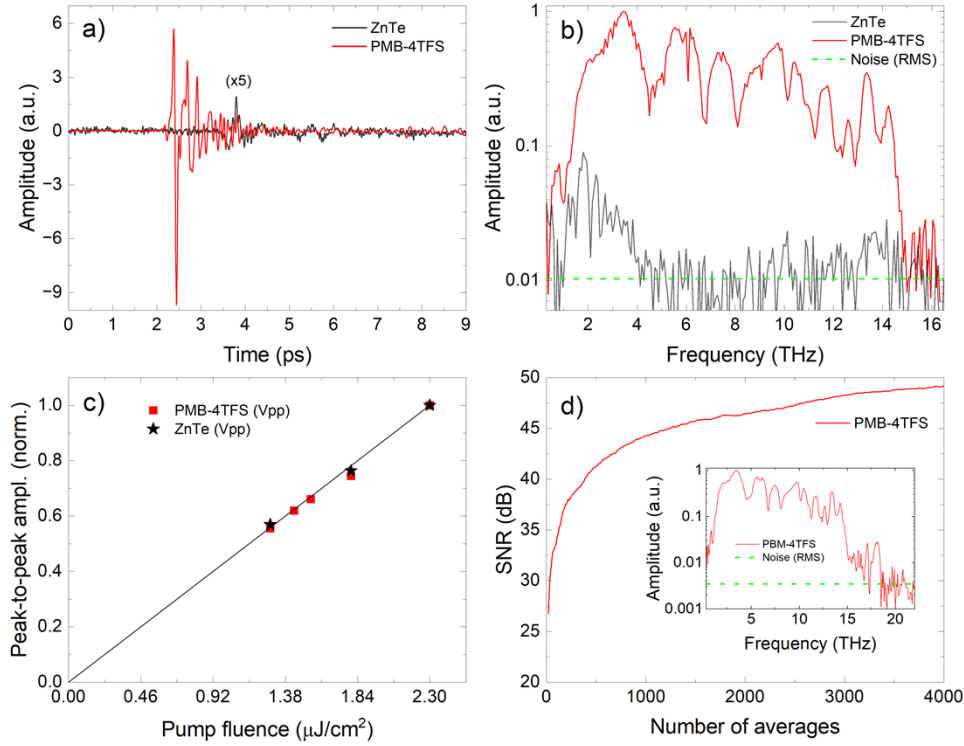


Fig. 4. (a) THz time-domain signal at normal incidence generated in a 0.29 mm thick PMB-4TFS and a 1.0 mm thick ZnTe crystals at a 1560 nm optical pump. Note that the amplitude of ZnTe was multiplied by a factor of 5 due to better representation; the measured peak-to-peak THz amplitude is for PMB-4TFS ~ 26 times higher than for ZnTe. (b) Spectra of the measured time-domain signals (Fourier transform of the signals shown in (a)). The PMB-4TFS spectrum has approximately one order of magnitude higher peak THz amplitude and covers a much broader THz frequency range in comparison to ZnTe. (c) Peak-to-peak amplitude, normalized for each crystal to value at the maximum fluence of $2.3 \mu\text{J}/\text{cm}^2$, of the generated THz signal vs. the pump fluence. The linear function (black line) shows that the THz field increases linearly with the fluence. (d) Signal-to-noise ratio (SNR) is increasing with the number of averages. The inset shows the spectrum obtained after 4000 averages.

the angle between the c axis, i.e., our experimental optical/THz polarization, and the optimal dielectric Z axis (the polar axis) of $\psi = 34.8^\circ$, the optimal cut would improve the amplitude of the generated THz field by about 80 percent (i.e., by a factor of $1/\cos^3\psi = 1.8$, see Eq. (1) below). However, cutting the PMB-4TFS crystals may not be easy along the desired plane and an easier solution is to rotate the crystal with respect to the incoming beam direction as shown in Fig. 5(a). For positive angles of incidence as chosen in Fig. 5, the pump beam polarization direction within the crystal approaches the polar axis Z , and the effective nonlinear optical susceptibility $\chi_{\text{eff}}^{(2)}$ approaches the maximum value $\chi_{ZZZ}^{(2)}$ according to

$$\chi_{\text{eff}}^{(2)} = \chi_{ZZZ}^{(2)} \cos^3\phi = \chi_{ZZZ}^{(2)} \cos^3(\psi - \theta_{\text{IN}}) \quad (1)$$

where ϕ is the angle between the polar dielectric Z axis and the internal beam polarization, which is oriented at an angle θ_{IN} , the internal angle of incidence, from the sample plane. For more detailed and extended derivation for crystals with non-negligible off-diagonal susceptibility tensor elements see Ref. [16]. Neglecting other factors such as changes in phase matching and

an increased beam propagation length, the generated THz field amplitude is directly proportional to the effective nonlinear optical susceptibility $\chi_{\text{eff}}^{(2)}$ and reaches its maximum at $\phi = 0^\circ$, which is equivalent to the situation for an optimally cut crystal. As shown in Fig. 5(b), already for angles $\theta_{\text{IN}} > 20^\circ$, more than 90% of the optimal amplitude generation efficiency can be reached. For a possible refractive index of 1.8 ± 0.2 (estimation based on the values from other red-color organic crystals [23]), this corresponds to external angles of incidence of above $38^\circ \pm 5^\circ$. Note that in previous THz generation measurements at 1 kHz repetition rate an external angle of incidence of 45° has been employed, resulting in a 36 times higher amplitude compared to that of the 1.0 mm thick ZnTe crystal [13], confirming an increase compared to the normal incidence configuration.

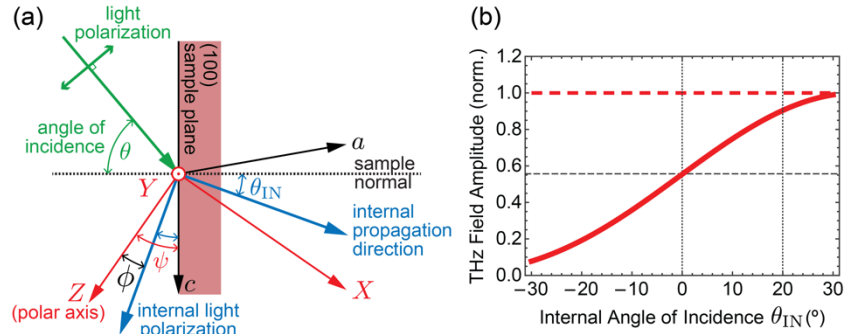


Fig. 5. (a) Geometry for THz-wave generation in PMB-4TFS at oblique light incidence. (b) Theoretically expected THz field amplitude according to Eq. (1) as a function of the internal angle of incidence θ_{IN} , normalized to the maximum value for the optimally cut crystal (100%, dotted red horizontal line).

4. THz absorption characteristics

The long molecular axes of PMB molecular cations and TFS molecular anions in PMB-4TFS crystals are anisotropically aligned with a small angle to the polar axis (Fig. 3). Therefore, PMB-4TFS crystals are expected to show a strong optical anisotropy in both optical and THz regions. This is because the linear (and the nonlinear) dielectric polarizability is for organic push-pull π -conjugated molecules like the PMB cation in this work much larger along the long molecular axis compared to the directions normal to it. This allows for an easy determination of the crystallographic c and b axis for as-grown (100) PMB-4TFS crystals using polarized light. For visible light polarized along the c axis, the crystal appears considerably darker in transmission compared to light polarized along the b axis, which is because of a small projection of the molecular axes along the b axis (Fig. 3(c)). This axis determination was confirmed also by a THz generation experiment, where practically no THz waves were generated by using pump polarization along the b axis. We also measured the absorption properties in the THz frequency region by using a broadband THz-TDS system as described in Ref. [19] by using an optimized 0.70 mm thick DSTMS for THz wave generation and the above-mentioned 0.76 mm DSTMS crystal for THz detection. We measured the transmission of a PMB-4TFS sample by scanning a 13.3 ps long time range at the resolution of 2 fs, a speed of 300 $\mu\text{m/s}$ and 50 averages and compared it to a reference signal acquired in dry air at the same parameters. Figure 6 shows the resulting absorbance of a 0.11 mm thick PMB-4TFS crystal along the crystallographic b and c axis in the frequency range up to 14.5 THz. The phonon absorption peak in the DSTMS generation and detection crystal at around 8.1 THz limits the measurement performance around this frequency and could therefore not be reliably measured. For the absorption peak at ~ 13 THz, the detection is limited by the maximum absorbance limit of the THz-TDS system shown by

the solid grey curve. PMB-4TFS crystals exhibit strong optical anisotropy in the overall THz frequency region. The absorption along the *b* axis is remarkably smaller than along the *c* axis. Many absorption peaks appear along the *c* axis; 4.5, 6.8, 10.1, 11.2, 12.4, 13.0, and 13.9 THz. In contrast, one stronger absorption peak and two weaker absorption peaks appear along the *b* axis. The observed strong anisotropy can be attributed to the highly ordered alignment of the PMB chromophores along the polar axis with a negligible projection of their long molecular axis along the *b* axis (see Fig. 3(c)).

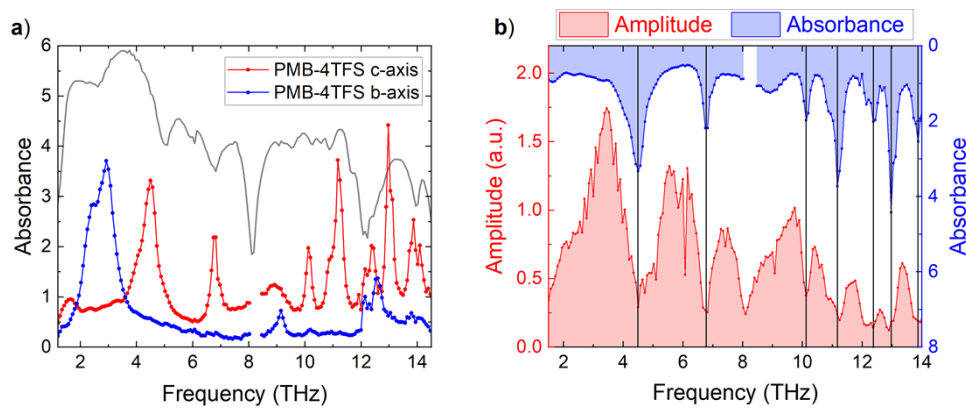


Fig. 6. (a) The absorbance of a 0.11 mm thick PMB-4TFS single crystal along the crystallographic *c* and *b* axis in the 1–14.5 THz frequency range. The solid grey curve represents the maximum absorbance limit of the THz-TDS system for this measurement. (b) THz generation spectrum (same as Fig. 4(b) but in the linear scale) and the absorbance (Fig. 6(a)), both along the *c* axis of PMB-4TFS crystals with a thickness of 0.29 mm and 0.11 mm, respectively.

The position of the absorption peaks along the *c* axis in the broad THz frequency range is well correlated with the position of dimples in the generated THz spectra. As shown in Fig. 6(b), the position of the absorption peaks marked with black vertical lines corresponds well to the position of dimples in the generated THz spectra. Few other broader dimples (e.g., at about 8.1 THz) are due to the absorption peaks in the detector DSTMS crystal [19], while most narrower oscillations in the amplitude can be attributed to residual water vapor absorption peaks at the experimental conditions (relative humidity of about 2%).

The THz-TDS measurements can be also used to evaluate the refractive index and the absolute values for the absorption coefficient of PMB-4TFS crystals along the *b*- and *c*-axis, using conventional evaluation procedure (see e.g. Reference [24]). The results are shown in Fig. 7, showing a strong birefringence with a considerably lower refractive index along the *b*-axis (except at around 2 THz due to the very strong phonon mode along the *b*-axis). The strong birefringence is again in agreement with the highly ordered alignment of PMB chromophores shown in Fig. 3(c), i.e., a high linear polarizability along the long molecular axis of the chromophores.

To investigate THz absorption characteristics at even higher frequencies, the transmittance of PMB-4TFS powders was measured using KBr pellets and a conventional FT-IR spectrometer. For comparison, PMB-T (2-(4-(4-(hydroxymethyl)piperidin-1-yl)styryl)-3-methylbenzo-thiazol-3-ium 4-methylbenzenesulfonate) [14] containing an identical PMB cation but a different anion was also examined. Figure 8 shows the absorption of PMB-4TFS powder in the range of 12–30 THz. In PMB-4TFS, the peaks at about 12.4, 12.9, and 13.8 THz in Fig. 8 appear at about the same position in the absorbance curves of the *b* and the *c* axis in Fig. 6(a), which confirms the reliability of both absorption measurements.

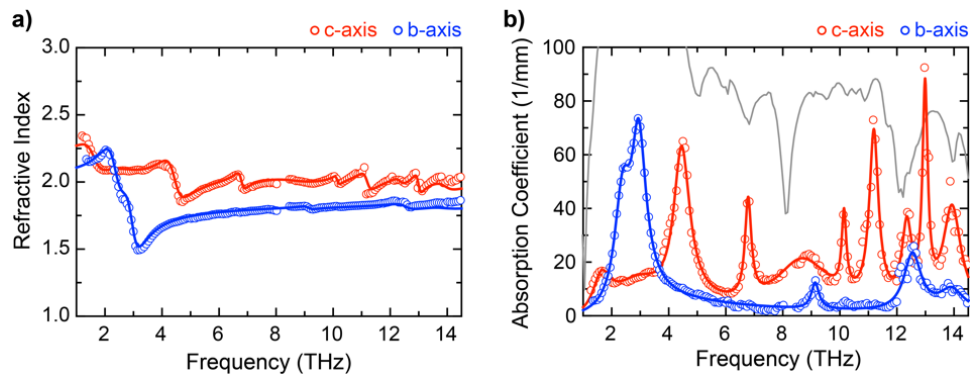


Fig. 7. (a) The refractive index n and (b) the absorption coefficient α for PMB-4TFS in the broadband THz frequency range, for the THz field polarization along the c - (red) and the b -axis (blue). The solid blue and red curves are according to a Lorentz oscillator model with several absorption peaks with the same parameters for both n and α for each polarization direction. The grey curve in (b) presents the absorption coefficient limit similarly as Fig. 6(a) for the absorbance.

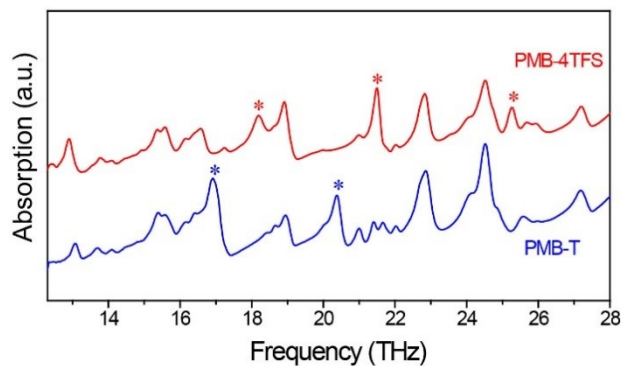


Fig. 8. Absorption (1-transmittance) of PMB-4TFS and PMB-T powders in the higher THz frequency range.

The red stars for PMB-4TFS and the blue stars for PMB-T denote representative non-overlapping peaks of these two materials. Assuming that intermolecular (interionic) interactions are not strongly involved in the molecular vibrational absorption spectrum above 12 THz, the red stars may be related to the TFS anion, and the blue stars may be related to the T anion. This assumption follows from previous periodic density functional theory calculations of organic THz salt crystals based on styryl cationic chromophores, for that the vibrations at higher frequencies near 12 THz originate solely from intramolecular vibrations [25]. Therefore, in PMB-4TFS, the influence of intermolecular interactions on most vibration modes at high THz frequency (e.g., 12–30 THz) may also be smaller than at low THz frequency. Interestingly, three peaks of PMB-4TFS presented with red stars at 18.2, 21.5, and 25.3 THz are observed at a practically identical position in another styryl-based ionic crystal HMQ-4TFS (2-(4-hydroxy-3-methoxystyryl)-1-methylquinolinium 4-(trifluoromethyl)benzenesulfonate) at 18.1, 21.7, and 25.4 THz [26]. In addition, the two peaks of PMB-T presented with blue stars (16.9 and 20.4 THz) are also observed at a practically identical position in HMQ-T (2-(4-hydroxy-3-methoxystyryl)-1-methylquinolinium 4-methylbenzenesulfonate) at 17.0 and 20.3 THz [26,27]. Consequently, the vibrations denoted by red stars in Fig. 8 are attributed to the vibrations of the TFS anion and those denoted by blue stars

to the vibrations of the T anion. The vibrations that appear at the same position for PMB-4TFS and PMB-T may be on the other hand related to intramolecular vibrations of the PMB cation. This shows that many absorption peaks of styryl-based crystals in the higher THz frequency range of 12–28 THz depend mainly on the chemical structure, rather than intermolecular interactions that are dominant in the lower THz frequency range. Note that since the PMB cation is non-analogous to the cations in HMQ-4TFS and HMQ-T, future work will be needed to identify the details of the vibrational modes, e.g., with periodic density functional theory calculations.

5. Thermochemical characteristics

The thermochemical characteristics of organic NLO crystals for THz wave generation are important for defining the possible upper and lower operating temperatures with thermal phase stability and long-term temporal stability of organic THz generators. The thermal phase stability is determined by two material parameters; phase transition temperatures and intrinsic thermochemical stability limited by a thermal bond-breaking of the chemical structure of cations and anions. In organic NLO crystals, phase transitions such as first-order melting transition appear usually above room temperature, and solid-to-solid phase transitions may also occur. Many organic NLO crystals that are candidates for organic THz generators show a moderately high melting temperature T_m (< 120 °C) [12], which limits the upper operating temperature [28–30]. If thermal bond-breaking decomposition temperature T_d appears below the melting temperature T_m , the upper operating temperature is the decomposition temperature T_d . In a few organic NLO crystals, a solid-to-solid phase transition may occur above room temperature below T_m and T_d [31], which then additionally lowers the upper operating temperature. The absence of solid-solid phase transition temperature below room temperature is also beneficial. This is because the low-temperature operation of THz generators is helpful to suppress the self-absorption of THz waves. When the operating temperature of organic THz generators is lowered, the generated THz amplitude increases by suppressing molecular phonon vibrations [32].

As discussed above, all phase-transition and decomposition temperatures below and above room temperature are important in practical THz applications. Figure 9 shows a differential scanning calorimetry (DSC) thermodiagram in a wide temperature range from -150 °C to $+284$ °C. Above room temperature (i.e., the usual operating temperature of THz generators), the lowest phase transition temperature is the melting temperature T_m at about 250 °C. The chemical decomposition happens at the same time as the melting transition; a strong exothermic peak appears just after the strong endothermic peak. As shown in Fig. 9, no phase transition appears below room temperature and above room temperature up to the melting temperature T_m . Consequently, the upper and the lower operating temperature of PMB-4TFS THz generators is about 250 °C and at least below -150 °C, respectively.

Many other benchmark organic NLO crystals are also based on styryl-based cationic chromophores [3]. In addition, in many widely used styryl-based organic NLO salt crystals, the chemical decomposition is strongly correlated with the melting transition and thermal stability. However, the thermochemical characteristics of styryl-based organic NLO crystals have not been extensively investigated yet. Only a few studies for photo-induced decomposition pathways have been suggested [33,34]. Note that the chromophores possessing high photochemical stability, important for THz applications due to the application of high-energy femtosecond laser pulses, may also have high thermal stability, i.e., high damage threshold against thermal decomposition.

In this work, we investigate the thermochemical characteristics of PMB-4TFS crystals as a model for widely used styryl-based chromophores by simultaneous thermal analysis and mass spectroscopy (STA-MS). PMB-4TFS single crystals were analyzed by a commercial STA-MS spectrometer (STA 409pc, and QMS 403c from NETZSCH). First, for screening the target mass, the STA-MS diagram was measured within the temperature range of 47 °C to 409 °C with a scan

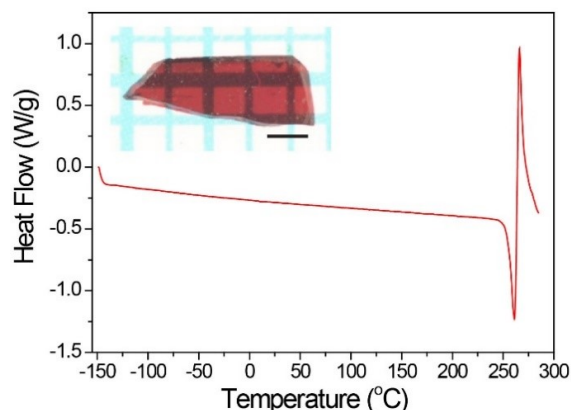


Fig. 9. Differential scanning calorimetry (DSC) thermodiagram of a PMB-4TFS single crystal in the low and the high-temperature range (heating scan rate: 10 °C/min) The inset is the photograph of the PMB-4TFS single crystal used in the DSC measurement (scale bar: 1 mm).

rate of 5 °C/min and a mass cycling time of about 24.8 sec/cycle in a mass range of 70–180 amu. In this analysis, 8 candidate groups with a mass range of 76–77, 81–82, 90–94, 104–108, 120–121, 134–136, 147–150, and 162–163 amu were selected. The candidate groups compared to unselected groups exhibit higher detection current value and higher numbers. After considering the possible and reasonable chemical species in thermochemical breaking down for PMB-4TFS crystals (see Fig. 10), we finally measured STA-MS with the mass range of 4 candidates 81–83, 133–136, 147–151, and 161–163 amu. For comparison, the mass of 140 amu was also measured.

Figure 10(a) shows the STA-MS diagram of PMB-4TFS crystals. The bond breaking of PMB-4TFS crystals is not a sequential process. At 235 °C, masses of all four candidate groups in the mass range of 81–83, 133–136, 147–151, and 161–163 amu simultaneously appeared. The three mass groups (133–136, 147–151, and 161–163 amu) originate from PMB cationic chromophores, as shown in Fig. 10(b). This indicates that the weakest bond in PMB cationic chromophores might be related to near the double bond that is a part of all styryl-based ionic and non-ionic chromophores. Interestingly, one mass group originating from the sulfonate group on 4TFS anions also simultaneously appeared along the three mass groups from PMB cationic chromophores. It seems that the thermochemical stability of styryl-based ionic and non-ionic chromophores and benzenesulfonate anions is limited to temperatures of about 235 °C. However, organic NLO salt crystals having styryl-based cationic chromophores and benzenesulfonate anions may exhibit much higher decomposition temperatures. For example, benzothiazolium HMB crystals with 4-methylbenzenesulfonate anion and quinolinium HMQ-T crystals exhibit higher decomposition temperature T_d of 297 °C [17,27] In addition, in PMB-based crystals, the melting temperature T_m and the decomposition temperature T_d are very close [14]. Therefore, the thermochemical stability is influenced also by the chemical structure of the electron donating group (i.e., that affects the electronic state of molecular orbitals) and the melting temperature (i.e., that depends on the strength of intermolecular interactions).

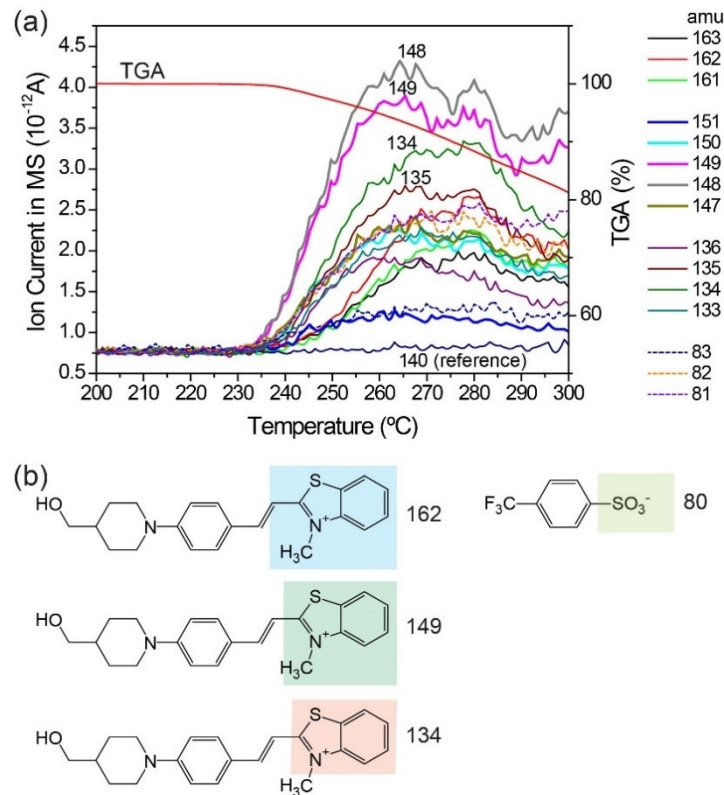


Fig. 10. (a) Simultaneous thermal analysis and mass spectroscopy (STA-MS) of PMB-4TFS crystals. (b) The chemical structure of 4 candidates in the mass range of 81–83, 133–136, 147–151, and 161–163 amu. The mass of 140 amu is a reference mass.

6. Conclusion

In this work, we demonstrated broadband THz wave generation based on benzothiazolium single crystals at a 100 MHz repetition rate. With PMB-4TFS benzothiazolium crystals we achieved a very high optical-to-THz conversion efficiency compared to ZnTe at 1560 nm pump laser wavelength. A 0.29 mm thick PMB-4TFS crystal generated broadband THz waves up to about ~15 THz and the generated THz electric field at normal incidence is ~26 times higher than in the inorganic standard, 1.0 mm thick ZnTe crystal at identical experimental conditions. Absorption characteristics and the anisotropy of the PMB-4TFS in the broad THz frequency range up to 28 THz were characterized by THz-TDS and FT-IR and the results are well correlated with the generated THz spectra. In addition, we investigated the thermochemical stability and degradation mechanisms of PMB-based single crystals by thermal analysis and mass spectroscopy, demonstrating a large possible operating temperature range of PMB-4TFS of at least between -150 °C and $+235$ °C.

Funding. Schweizerischer Nationalfonds zur Förderung der Wissenschaftlichen Forschung (IZKSZ2_188194); National Research Foundation of Korea (2019K1A3A1A14057973, 2021R1A2C1005012, 2021R1A5A6002853).

Disclosures. The authors declare no conflicts of interest.

Data availability. Data underlying the results presented in this paper may be obtained from the authors upon reasonable request.

References

1. H. A. Hafez, X. Chai, A. Ibrahim, S. Mondal, D. Férachou, X. Ropagnol, and T. Ozaki, "Intense terahertz radiation and their applications," *J. Opt.* **18**(9), 093004 (2016).
2. J. A. Spies, J. Neu, U. T. Tayvah, M. D. Capobianco, B. Pattengale, S. Ostresh, and C. A. Schmuttenmaer, "Terahertz spectroscopy of emerging materials," *J. Phys. Chem. C* **124**(41), 22335–22346 (2020).
3. S.-J. Kim, B. J. Kang, U. Puc, W. T. Kim, M. Jazbinsek, F. Rotermund, and O.-P. Kwon, "Highly nonlinear optical organic crystals for efficient terahertz wave generation, detection, and applications," *Adv. Opt. Mater.* **9**(23), 2101019 (2021).
4. C.-U. Jeong, B. J. Kang, S.-H. Lee, S.-C. Lee, W. T. Kim, M. Jazbinsek, W. Yoon, H. Yun, D. Kim, F. Rotermund, and O.-P. Kwon, "Yellow-colored electro-optic crystals as intense terahertz wave sources," *Adv. Funct. Mater.* **28**(30), 1801143 (2018).
5. J. Buldt, H. Stark, M. Müller, C. Grebing, C. Grebing, C. Jauregui, J. Limpert, J. Limpert, and J. Limpert, "Gas-plasma-based generation of broadband terahertz radiation with 640 mW average power," *Opt. Lett.* **46**(20), 5256–5259 (2021).
6. T. S. Seifert, L. Cheng, Z. Wei, T. Kampfrath, and J. Qi, "Spintronic sources of ultrashort terahertz electromagnetic pulses," *Appl. Phys. Lett.* **120**(18), 180401 (2022).
7. E. T. Papaioannou and R. Beigang, "THz spintronic emitters: a review on achievements and future challenges," *Nanophotonics* **10**(4), 1243–1257 (2021).
8. J. Liu, C. Ouyang, F. Huo, W. He, and A. Cao, "Progress in the enhancement of electro-optic coefficients and orientation stability for organic second-order nonlinear optical materials," *Dyes Pigm.* **181**, 108509 (2020).
9. G. A. Valdivia-Berroeta, Z. B. Zaccardi, S. K. F. Pettit, (Enoch) Sin-Hang Ho, B. W. Palmer, M. J. Lutz, C. Rader, B. P. Hunter, N. K. Green, C. Barlow, C. Z. Wayment, D. J. Ludlow, P. Petersen, S. J. Smith, D. J. Michaelis, and J. A. Johnson, "Data Mining for Terahertz Generation Crystals," *Adv. Mater.* **34**(16), 2107900 (2022).
10. G.-E. Yoon, J.-H. Seok, U. Puc, B.-R. Shin, W. Yoon, H. Yun, D. Kim, I. C. Yu, F. Rotermund, M. Jazbinsek, and O.-P. Kwon, "Phonon-suppressing intermolecular adhesives: catechol-based broadband organic THz generators," *Adv. Sci.* **9**(24), 2201391 (2022).
11. G. A. Valdivia-Berroeta, I. C. Tangen, C. B. Bahr, K. C. Kenney, E. W. Jackson, J. DeLagange, D. J. Michaelis, and J. A. Johnson, "Crystal growth, terahertz generation, and optical characterization of EHPSI-4NBS," *J. Phys. Chem. C* **125**(29), 16097–16102 (2021).
12. G. Montemezzani, C. Medrano, M. Zgonik, and P. Günter, "The photorefractive effect in inorganic and organic materials," in *Nonlinear Optical Effects and Materials*, P. Günter, ed., Springer Series in Optical Sciences (Springer, 301–373 (2000).
13. D. Kim, W. T. Kim, J.-H. Seok, I. C. Yu, M. Jazbinsek, W. Yoon, H. Yun, D. Kim, F. Rotermund, and O.-P. Kwon, "Molecular salt crystals with bis(head-to-tail) interionic complementary assembly for efficient organic THz generators," *J. Mater. Chem. C* **8**(29), 10078–10085 (2020).
14. S.-C. Lee, B. J. Kang, J.-A. Lee, S.-H. Lee, M. Jazbinšek, W. Yoon, H. Yun, F. Rotermund, and O.-P. Kwon, "Single crystals based on hydrogen-bonding mediated cation–anion assembly with extremely large optical nonlinearity and their application for intense THz Wave generation," *Adv. Opt. Mater.* **6**(10), 1701258 (2018).
15. S.-J. Kim, I. C. Yu, J.-A. Lee, W. T. Kim, M. Jazbinsek, W. Yoon, H. Yun, F. Rotermund, and O.-P. Kwon, "New benzothiazolium crystals with very large off-diagonal optical nonlinearity," *Dyes Pigm.* **192**, 109433 (2021).
16. J.-A. Lee, W. T. Kim, M. Jazbinsek, D. Kim, S.-H. Lee, I. C. Yu, W. Yoon, H. Yun, F. Rotermund, and O.-P. Kwon, "X-shaped alignment of chromophores: potential alternative for efficient organic terahertz generators," *Adv. Opt. Mater.* **8**(9), 1901921 (2020).
17. S.-H. Lee, J. Lu, S.-J. Lee, J.-H. Han, C.-U. Jeong, S.-C. Lee, X. Li, M. Jazbinšek, W. Yoon, H. Yun, B. J. Kang, F. Rotermund, K. A. Nelson, and O.-P. Kwon, "Benzothiazolium single crystals: a new class of nonlinear optical crystals with efficient thz wave generation," *Adv. Mater.* **29**(30), 1701748 (2017).
18. J. Zyss and J. L. Oudar, "Relations between microscopic and macroscopic lowest-order optical nonlinearities of molecular crystals with one- or two-dimensional units," *Phys. Rev. A* **26**(4), 2028–2048 (1982).
19. U. Puc, T. Bach, P. Günter, M. Zgonik, and M. Jazbinsek, "Ultra-broadband and high-dynamic-range THz time-domain spectroscopy system based on organic crystal emitter and detector in transmission and reflection geometry," *Adv. Photonics* **2**(4), 2000098 (2021).
20. Z. Yang, L. Mutter, M. Stillhart, B. Ruiz, S. Aravazhi, M. Jazbinsek, A. Schneider, V. Gramlich, and P. Günter, "Large-size bulk and thin-film stilbazolium-salt single crystals for nonlinear optics and THz generation," *Adv. Funct. Mater.* **17**(13), 2018–2023 (2007).
21. T. O. Buchmann, E. J. Railton Kelleher, M. Jazbinsek, B. Zhou, J.-H. Seok, O.-P. Kwon, F. Rotermund, and P. U. Jepsen, "High-power few-cycle THz generation at MHz repetition rates in an organic crystal," *APL Photonics* **5**(10), 106103 (2020).
22. T. O. Buchmann, T. O. Buchmann, E. J. R. Kelleher, K. J. Kaltenecker, B. Zhou, S.-H. Lee, O.-P. Kwon, M. Jazbinsek, F. Rotermund, P. U. Jepsen, and P. U. Jepsen, "MHz-repetition-rate, sub-mW, multi-octave THz wave generation in HMQ-TMS," *Opt. Express* **28**(7), 9631–9641 (2020).
23. M. Jazbinsek, U. Puc, A. Abina, and A. Zidansek, "Organic crystals for THz photonics," *Appl. Sci.* **9**(5), 882 (2019).
24. P. U. Jepsen, "Phase retrieval in terahertz time-domain measurements: a "how to" tutorial," *J. Infrared, Millimeter, Terahertz Waves* **40**(4), 395–411 (2019).

25. J. Kim, Y. C. Park, J.-H. Seok, M. Jazbinsek, and O.-P. Kwon, "Solid-state molecular motions in organic THz generators," *Adv. Opt. Mater.* **9**(4), 2001521 (2021).
26. S.-H. Lee, B. J. Kang, B.-W. Yoo, S.-C. Lee, S.-J. Lee, M. Jazbinsek, H. Yun, F. Rotermund, and O.-P. Kwon, "Terahertz phonon mode engineering of highly efficient organic terahertz generators," *Adv. Funct. Mater.* **27**(14), 1605583 (2017).
27. P.-J. Kim, J.-H. Jeong, M. Jazbinsek, S.-B. Choi, I.-H. Baek, J.-T. Kim, F. Rotermund, H. Yun, Y. S. Lee, P. Günter, and O.-P. Kwon, "Highly efficient organic THz generator pumped at near-infrared: quinolinium single crystals," *Adv. Funct. Mater.* **22**(1), 200–209 (2012).
28. F. D. J. Brunner, A. Schneider, and P. Günter, "Velocity-matched terahertz generation by optical rectification in an organic nonlinear optical crystal using a Ti:sapphire laser," *Appl. Phys. Lett.* **94**(6), 061119 (2009).
29. L. Du, F. Roeder, Y. Li, M. Shalaby, B. Beleites, F. Ronneberger, and A. Gopal, "Organic crystal-based THz source for complex refractive index measurements of window materials using single-shot THz spectroscopy," *Appl. Phys. A* **127**(11), 846 (2021).
30. I. C. Tangen, G. A. Valdivia-Berroeta, L. K. Heki, Z. B. Zaccardi, E. W. Jackson, C. B. Bahr, (Enoch) Sin-Hang Ho, D. J. Michaelis, D. J. Michaelis, J. A. Johnson, and J. A. Johnson, "Comprehensive characterization of terahertz generation with the organic crystal BNA," *J. Opt. Soc. Am. B* **38**(9), 2780–2785 (2021).
31. O.-P. Kwon, S.-J. Kwon, M. Jazbinsek, A. Choubey, V. Gramlich, and P. Günter, "New organic nonlinear optical polyene crystals and their unusual phase transitions," *Adv. Funct. Mater.* **17**(11), 1750–1756 (2007).
32. A. G. Stepanov, C. Ruchert, J. Levallois, C. Erny, and C. P. Hauri, "Generation of broadband THz pulses in organic crystal OH1 at room temperature and 10 K," *Opt. Mater. Express* **4**(4), 870–875 (2014).
33. A. Galvan-Gonzalez, K. D. Belfield, G. I. Stegeman, M. Canva, S. R. Marder, K. Staub, G. Levina, and R. J. Twieg, "Photodegradation of selected π -conjugated electro-optic chromophores," *J. Appl. Phys.* **94**(1), 756–763 (2003).
34. D. Rezzonico, M. Jazbinsek, P. Günter, C. Bosshard, D. H. Bale, Y. Liao, L. R. Dalton, and P. J. Reid, "Photostability studies of π -conjugated chromophores with resonant and nonresonant light excitation for long-life polymeric telecommunication devices," *J. Opt. Soc. Am. B* **24**(9), 2199–2207 (2007).